# Naturally architected microstructures in structural materials via additive manufacturing

Kellen D. Traxel and Amit Bandyopadhyay\*
W. M. Keck Biomedical Materials Research Laboratory
School of Mechanical and Materials Engineering
Washington State University, Pullman, WA 99164, USA
\*E-mail: amitband@wsu.edu

#### Abstract

Despite recent advances in our understanding of the unique mechanical behavior of natural structural materials such as nacre and human bone, traditional manufacturing strategies limit our ability to mimic such nature-inspired structures using existing structural materials and manufacturing processes. To this end, we introduce a customizable single-step approach for additively fabricating geometrically-free metallic-based structural composites showing directionally-tailored, location-specific properties. To exemplify this capability, we present a layered metal-ceramic composite not previously reported exhibiting significant directional and site-specific dependence of properties along with crack arrest ability difficult to achieve using traditional manufacturing approaches. Our results indicate that nature-inspired microstructural designs towards directional properties can be realized in structural components using a novel additive manufacturing approach.

<u>Keywords:</u> natural design, hybrid materials, structural materials, additive manufacturing, titanium, niobium carbide

#### Introduction

In every structural application, material-based design compromises are made to accommodate cost and processability of materials, need for complex geometries, and reduced component mass, among other metrics that drive the design-cycle. To overcome such compromises, a distinct focus is being paid towards advanced techniques that combine unique processing flexibility, a wide range of materials, and the ability to tailor components for application-specific needs. One area that can provide some design inspiration is the strategies

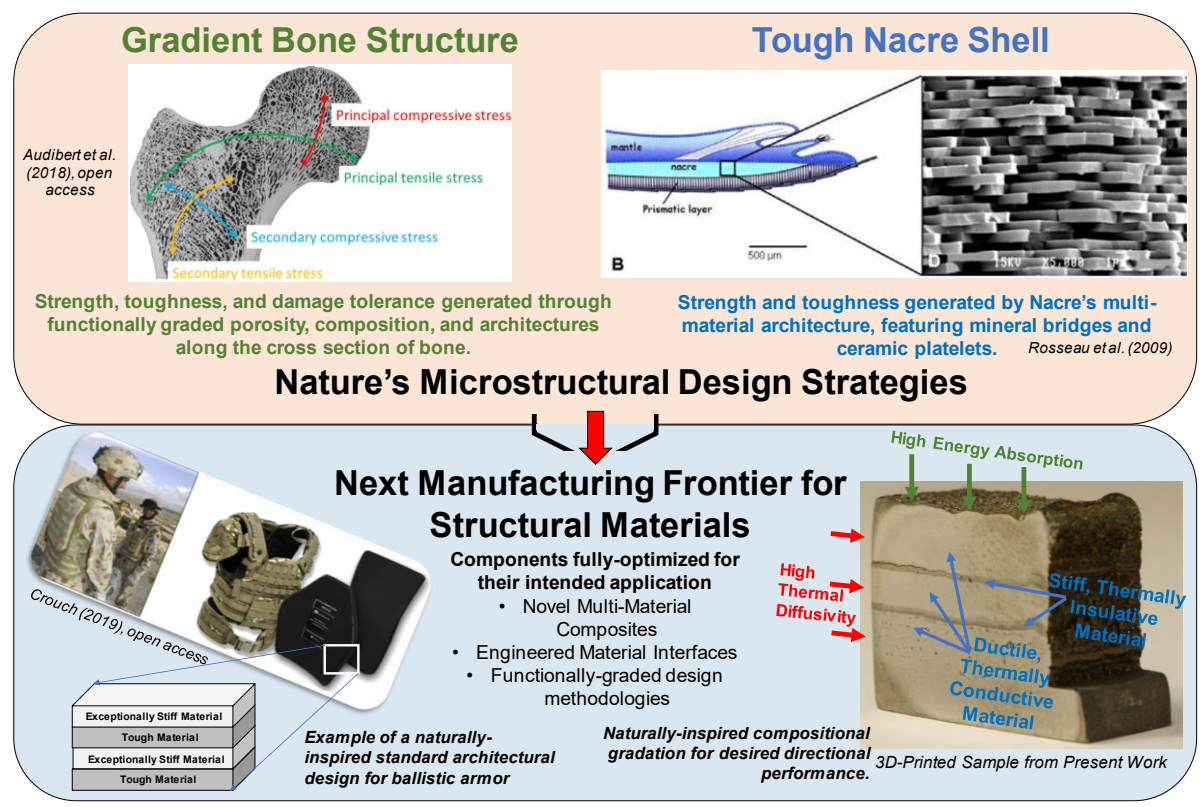


**Figure 1:** Human bone and nacre as examples of strong, yet tough materials that can inspire the next generation of metallic-based composite structures [3,4].

that natural structures (**Figure** 1) have developed to combine properties such as strength and stiffness in single structures to provide superior properties in comparison to the base constituents, and reduced overall required mass to achieve such properties [1–4]. Although much of the underlying mechanisms have been elucidated in complex materials such as bone and nacre, there remains significant opportunity to translate these concepts into real application (see **Figure 1**) [5]. From a design perspective, bone's damage tolerance originates from intrinsic toughening generated by the allowed plastic deformation of fibrils that slide against one another between mineral platelets, enabling load to be transferred from one platelet to another while resisting complete failure [2]. Additionally, bone's functionally graded architecture provides both load transfer capability as well as biological functionality, i.e., cancellous (inner porous portion) provides porous areas of high vascularization and cortical (outside) bone provides regions of higher stiffness and extrinsic crack deflection/twist capability to avoid fracture [1]. In nacre (or abalone shell), mineral bridges serve as a "cement" to enable plastic deformation and transfer of load between mineral platelets, enabling a strong, yet tough, microstructure [1,2,6]. From these,

it is clear that nature has evolved to create structures that are completely optimized for their intended environment by a combination of compositional and architectural variation within single components. With the constant challenge of creating improved metal alloys and composites for numerous applications, it is envisioned that the development of manufacturing techniques that can create these multi-functional, and challenging structures will greatly enhance our ability to increase performance characteristics such as strength, stiffness, and toughness, among many others, to open new design frameworks for architected materials.

Additive manufacturing (AM) or 3D Printing, a layer-by-layer processing technology, has enabled researchers to explore new concepts and manufacturing routes while decreasing the amount of compromises made in the design process, and is a budding technology for the development of architected structures and materials [7–10]. The AM technology platform has stimulated the individual development of improved engineering alloys [11], multi-material and functionally-graded materials [8,12], lattice and topology-optimized structures [13], and metalmatrix composites and coatings [14,15]. While these frontiers are exciting, the next generation relies on developing techniques that enable structures to be crafted from their intended operational environment, as is the case with natural materials, and are not based on the available fabrication processes [16,17]. These situations often occur in ballistic armor design (see **Figure** 1) [18–20], pressure vessels [21], and thermal barrier coatings [22], among others, requiring structures with site-specific composition to achieve directional electrical/thermal properties, ductility, and strength, among others, and typically require the use of both structural metals and reinforcing ceramic phases. Traditional processes such as tape casting, reaction bonding, thermal spraying, and powder metallurgy, among others, have been utilized to manufacture some of these structures, all exhibiting limitations for the possible final geometries and/or processing complexity as well as cost [18,19,23,24]. The current difficulty associated with integrating design, manufacturing, and performance warrants the investigation of novel, alternative fabrication methods for these types of structures, as well as developing frameworks for design.

To this end, we detail a manufacturing framework for naturally-inspired, directionally-optimized, metal-ceramic composites by means of an alternating-material deposition AM technique not previously reported (See **Fig. 2**). In other works, metals and ceramics have been processed via laser-based techniques in a functionally-graded or coating-based manner where

metal transitions to a ceramic or metal-ceramic composition [25–27], however, the key novelty in our work resides in laser-processing of structures that begin with metal, transition to ceramic, and then transition back to metal again in a way that produces a hierarchically layered, ribbon-

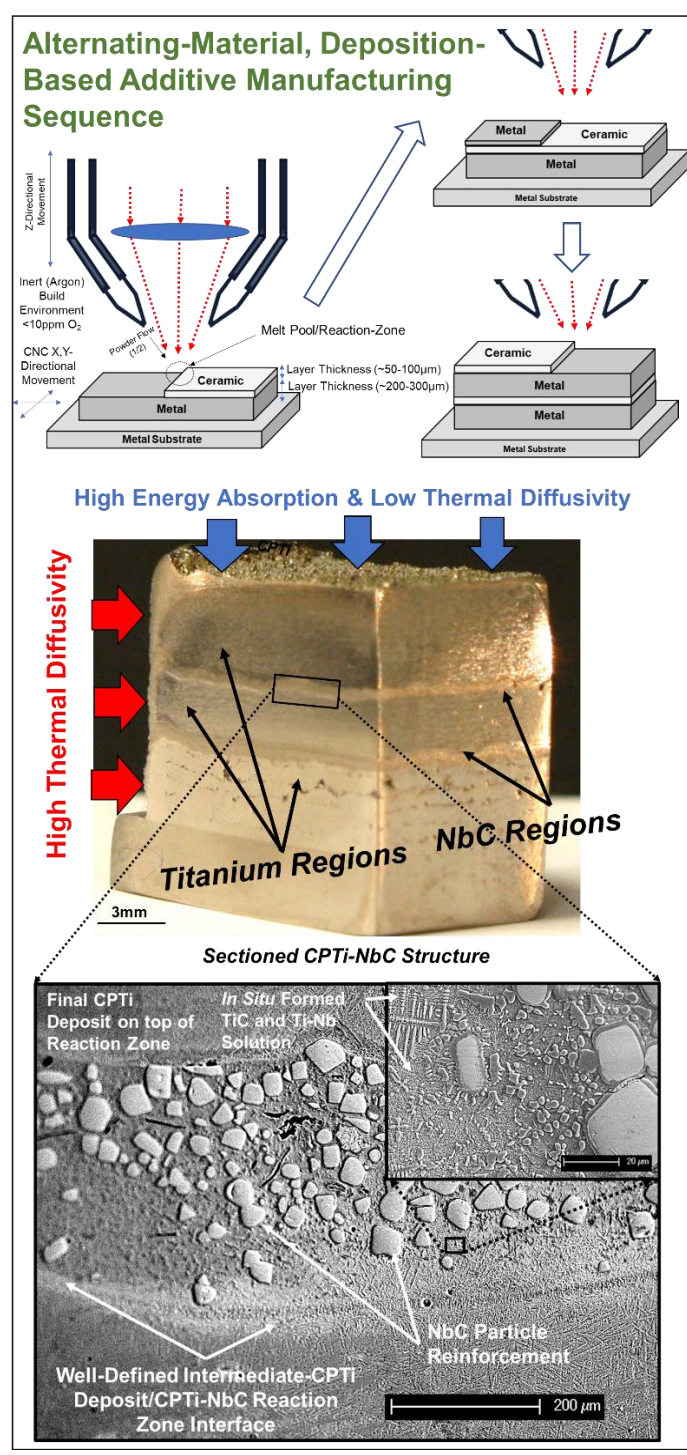


**Figure 2:** Illustrative schematic of alternating-material deposition process and the unique layering and microstructural characteristics.

like structure capable of directionalload carrying capabilities, inspired by natural multi-material structures such as nacre and bone. Particularly in the case of blunt-impact armor backing metalceramic materials, designs have typically been limited to a hard steel or ceramic outer design, owing to the combination of blunt impact resistance, manufacturability, and crack arrest capability [28]. Because high-strength and low-density are the ideal materials of choice for these high kinetic energy impacts [29], investigation of processing and properties of different reinforced metal-ceramic composite materials have become extensive, but there still remains significant processing challenges which open the door to new fabrication and design methodologies [30]. If naturally-inspired layered metalceramic composites are produced via alternating-material-deposition technique, these structures can be fabricated in a single step that would save significant cost and time, while opening new design possibilities to researchers and engineers. The key

knowledge gap in the literature lies in both an understanding of the possibility of manufacturing these structures using additive-based processes, as well as how in situ phase formations and layering designs can influence achievable properties. To demonstrate the ability to fabricate such a structure, we utilize a directed-energy-deposition (DED) based AM approach with alternating laser-deposition of a ductile, thermally conductive matrix phase, commercially-pure titanium (CPTi), and an insulative, stiff reinforcing phase in niobium carbide (NbC). Titanium, known for its high strength/weight ratio, corrosion resistance, and biocompatibility, and niobium carbide, a refractory ceramic with high strength and stiffness, have been printed in different composite systems previously, [31,32] but were chosen together to demonstrate the possibility of combining their unique properties such as stiffness, strength, and thermal diffusivity. Although titanium and niobium (metal) have been printed previously for biomedical applications [33,34], literature on titanium and niobium-carbide (ceramic) printed together is limited, and therefore demonstrating the microstructural characteristics, phase evolution, and resulting properties would greatly advance our understanding of the processing capabilities of these two materials in addition to the unique nature of the layering schemes. We hypothesize that composite structures manufactured using alternating-material deposition exhibit properties that are both directionally-dependent and different from the starting materials, performing comparably to armor-based backing material designs, and imitating natural structural materials such as nacre and bone. A CPTi-3.5vol%NbC printed sample serves as a control for comparing a composite system of similar estimated NbC reinforcement to the directionally-tailored layered structures. This specific amount was chosen based on estimations of NbC reinforcement in the as-printed alternating-material structures, and this composition was processed via LENS<sup>TM</sup> to understand the differences between a premixed composite and a layered one with similar reinforcement amount. Compression damage evaluation and modified rule-of-mixtures analysis of thermomechanical behavior provides insight into how this process can be adjusted to further enhance performance. Our work demonstrates the ability to customize a commercial laser-based AM technique to create structures that are tailored to meet the needs of demanding applications.

## **Materials and Methods**

**Table 1:** Processing parameters for the initial as-printed structure as well as the final, optimized structure used for testing and analysis.

Sequence and Description			<u>Layers</u>	<u>Laser Power</u> (W)	Scan Speed (mm/s)	Hatch Spacing (mm)	<u>Layer</u> <u>Height</u> (μm)	Energy Density (J/mm³)
Initial	1	CPTi Deposition on Substrate	10	410		0.6	300	325
	2,4	NbC Deposition on CPTi	2	Layer 1: 410 Layer 2: 450	7		100	Layer 1: 975 Layer 2: 1075
	3,5	5 CPTi Deposition on NbC 4		410	)		300	325
Optimal	1	CPTi Deposition on Substrate	10	410		0.6	300	325
	2,4	NbC Deposition on CPTi	2	450	7		100	1075
	3,5	CPTi Deposition on NbC	10	410			300	325
CPTi-3.5vol%NbC (All Layers)			34	430	7	0.6	300	350

Note: Average layer thicknesses (425µm for CPTi, 100µm for NbC) are used for energy density calculations, as indicated from micrograph estimations (not shown).

Materials and processing technology: Our LENS<sup>TM</sup> system utilizes a continuous-wave Nd:YAG laser (500W) to melt a pool of deposited powder onto a substrate that moves in the x/y directions. The build platform is enclosed in a controlled argon environment (O<sub>2</sub> ppm<15) to

**Table 2:** Tabulated quasi-static compression and thermal diffusivity testing results.

<u>Parameter</u>	Longitudinal Configuration	<u>Transverse</u> <u>Configuration</u>	Premixed Configuration (CPTi-3.5vol%NbC)	
Compressive Yield Strength (MPa)	594 ± 6	538 ± 4	$750 \pm 57$	
Compressive Modulus (GPa)	$190 \pm 15$	$140 \pm 33$	$230 \pm 25$	
Theoretical Compressive Modulus (GPa)	149-162 GPa	122-125 GPa	165-210 GPa	
Percent Difference from Theoretical (%)	15 - 22%	11 - 13%	9 - 28%	
Average Thermal Diffusivity across 50°C-300°C (mm <sup>2</sup> /s)	$6.8 \pm 0.03$	$6.22 \pm 0.02$	$5.47 \pm 0.02$	
Percent Difference from Theoretical (%) across 50°C-300°C	0.7%- 9.2%	0.4% - 6.3%	0.2% - 16.2%	

<sup>\*</sup>All theoretical values come from composite structural theory expanded upon in the discussion section.

limit oxidation during high-temperature processing. The powder (metal or metal-ceramic composition) is carried into the melt pool via an argon stream. Further discussion of this technique can be found in references [35,36]. For this study, spherical CPTi powder (Gr.2 Ancor-Ti, Hoganas, Sweden), and granular-NbC powder (Companhia Brasileira de Metalurgica e Mineração, Brazil) were obtained for printing of the composite structures. Titanium powder was printed within a 45-150μm particle size range, and the NbC particles ranged from 25-75μm in overall size (as-received). The premixed composition was milled for 20 minutes, without balls, to ensure compositional homogeneity. All samples were 3D printed separately (Optomec LENS<sup>TM</sup> 750, Optomec, Albuquerque, NM) as 15mm by 25mm rectangular cross-sectional patterns, onto a 3.4mm thick CPTi substrate, according to the parameters outline in **Table 1**.

The volumetric energy density equation comes from investigations of both powder-bed and directed-energy-deposition systems[37–39], expressed as:

$$E = \frac{P}{vht} \quad (1)$$

Where P is input power (W), v is scan speed (mm/s), h is hatch spacing (mm), and t is layer thickness (mm).

<u>Sample preparation, microstructural characterization, and phase analysis</u>: After processing via alternating-material deposition technique, and before further testing, samples for

imaging and analysis (**Figs. 3 & 4**) were sectioned via low-speed diamond saw, mounted in phenolic resin, then sequentially wet-ground using 60-2000 grit SiC paper. Polishing was performed using an alumina-DI water suspension from 1μ down to 0.05μ. X-Ray Diffraction (XRD) (X'Pert PRO PANalytical, Almelo, Netherlands, Cu Kα source and a Ni filter) was performed for the as-printed, ground and polished, alternating-material specimens (**Fig. 4**). XRD peaks for phases are determined from the HighScore Plus software database (ICSD-cross referenced). All intensities were normalized by the largest peak observed. Vickers cross-section hardness indents (Phase II, Upper Saddle River, NJ) were taken in line with ASTM standards for both metals and advanced ceramics on the unetched, ground and polished cross sections (**Fig. 5A**) [40,41]. To understand the crack-arresting capabilities, a printed sample was ground down from the top surface into the reaction zone and several indents were made at a load of 1kg (schematic shown in **Fig. 5B**) High-magnification imaging, Field-Emission Scanning Electron Microscopy (FESEM, SEM) and Energy Dispersive Spectroscopy (EDS), (EDAX by Ametek, PA) were utilized on etched specimens. Submersion etching for 25s was done in Kroll's Solution (92mL DI Water, 6mL HNO<sub>3</sub>, & 2mL HF).

Thermomechanical testing: For the printed specimens, quasi-static compression testing (SHIMADZU Trapezium X, Kyoto, Japan) was performed at constant crosshead displacement rate of 0.15 mm/min (~0.2\*10<sup>-4</sup> s<sup>-1</sup> strain rate in linear region) until plastic deformation was evident from the live displacement vs. force output (**Figs. 6-8**). Two samples per configuration were ground to side-lengths of 5.25±0.05mm and height of 11.5±0.05mm for an average height to side-length ratio of ~2. No extensometer was used because of the small specimen size. Moduli were evaluated via the slope of the stress-strain curve in the linear region, and a standard 0.2% offset method was used for the yield strength of each configuration, per ref. [42]. Damage analysis was performed on a single as-compressed, unetched sample from each configuration (**Fig. 7**). Estimates for the moduli in the transverse loading direction are made using the Halpin-Tsai model for layered and fiber-reinforced composites[43]. This model is meant to capture the tendency of compressive deformation to be dominated by the matrix material, resulting in:

$$E_{Transverse} = \frac{E_M(1 + \zeta \eta v_{RZ})}{(1 - \eta v_{RZ})} \quad (2)$$

Where:

$$\eta = \frac{\left(\frac{E_{RZ}}{E_M}\right) - 1}{\left(\frac{E_{RZ}}{E_M}\right) + \zeta} \tag{3}$$

As above, the subscripts m and RZ refer to both matrix and reaction zone, respectively. A value of 2 was used for  $\zeta$  as it showed good agreement with experimental data for fiber-reinforced composites of reinforcement fractions most nearly 0.55 [43], and because this parameter showed minimal effect on the modulus estimation for this particular configuration. For the longitudinal and premixed compressive loading cases, a rule of mixtures approach is used, which is equivalent to Eq.8 for the effective conductivity. The premixed composition's variation is found by using the estimated  $\frac{\Delta R}{R}$  range of 1-1.5, as in the thermal diffusivity analysis.

For high strain-rate compression testing, a split-hopkinson pressure bar (SHPB) setup (**Fig. 9-10**) was used similar to that described and used in ref. [44]. Specimens from the premixed composition, longitudinal (only one layer) and the transverse (2 total layers) were used (n=2). Each sample was  $5.00\pm0.05$ mm in diameter and  $10.00\pm0.05$ mm in length. For testing, the engineering stress and strain are determined from the measurement of stress wave (both reflected ( $\epsilon_R$ ) and transmitted ( $\epsilon_T$ )) through the sample during impact and subsequent plastic deformation. A high-strength steel bar was used to ensure elastic behavior in the bar during specimen deformation. The striker bar velocity was held constant at 11m/s which resulted in strain rates of  $\sim$ 1-2\*10<sup>3</sup> s<sup>-1</sup> across each composition. The engineering strain rate is determined from the reflected wave as such:

$$\dot{\epsilon}_s(t) = \frac{2C_b}{l_s} \epsilon_R(t) \quad (4)$$

where  $l_s$  is the length of the specimen and  $C_b$  is the wave speed in the steel bar. From this information, the engineering-strain can be calculated from the integral:

$$\epsilon_s(t) = \int_0^t \dot{\epsilon}_s(t) dt \quad (5)$$

The engineering stress is determined from the transmitted bar as such:

$$\sigma(t) = \frac{E_b A_b}{A_c} \epsilon_T(t) \quad (6)$$

where  $E_b$ ,  $A_b$  are the modulus and cross-sectional area of the impactor, and  $A_s$  is the cross-sectional area of the specimen. Yield strengths were determined using the 0.2% offset method, and the total strain to failure was determined by the final failure of each specimen from withstanding a load (transverse and premixed), or when continued compaction of failed material was exhibited (longitudinal). Further discussion of this technique can be found from ref. [44].

Thermal diffusivity testing was performed via the flash method from 50°C-300°C (NETZSCH, Germany) on specimens measuring 10.4±0.5mm square and 2.5±0.05mm thickness. Prior to testing, a thin layer of graphite was applied on each side of the testing specimen to ensure measurement accuracy. Because of the limits on specimen thickness, only one reaction zone region was able to be tested, as is indicated schematically in **Fig. 6**. Theoretical values for additional reaction zones within the same 2.5mm thickness sample are shown in **Fig. 8**. Thermal diffusivity analysis of all structures is based on the following relation:

$$\alpha = \frac{k}{\rho C_P} \quad (7)$$

Where k is the effective conductivity of the structure (W/mK),  $\rho$  is the structure's density, and  $C_P$  is the specific heat (J/kgK), resulting in final units of (mm²/s). Temperature-dependent specific heat data for all phases came from ref [45]. For each of the alternating-material composites, k was estimated using a series-connected thermal circuit for the transverse configuration, and a parallel-connected thermal circuit for the longitudinal configuration[39,46]. This results in the following formulations after rearranging terms for the effective conductivity of the matrix  $(k_m)$ , reaction-zone reinforcement  $(k_{RZ})$ , and the ratio of the width/thickness of the CPTi-NbC reaction zone to the overall sample thickness  $(r_{RZ})$ :

$$k_{Transverse} = \frac{k_m k_{RZ}}{k_{RZ} (1 - r_{RZ}) + k_m (r_{RZ})} \tag{8}$$

And:

$$k_{Longitudinal} = k_m (1 - r_{RZ}) + k_{RZ}(r_{RZ}) \quad (9)$$

These equations can also be referred to as the inverse rule of mixtures and rule of mixtures, respectively. A standard rule-of-mixtures formulation was used for the premixed composition, similar to the longitudinal relation, but with the incorporation of an effective volume increase

factor due to the *in situ* formation of TiC and Ti-Nb solution, to account for the non-rule of mixtures behavior:

$$\frac{v_R}{v_{apparent}} = \left(1 + \frac{\Delta R}{R}\right)^3 \quad (10)$$

Where  $\frac{\Delta R}{R}$  represents the radial increase ratio from particle to particle-*in situ* phase reinforcement.

## **Results and Discussion**

Structure fabrication was carried out as shown schematically in Fig. 2, depositing one powder at a time. Titanium metal powder was first printed on the substrate at 325 J/mm³ input energy (see Table 1), and then a sequence of alternating ceramic NbC phase and Ti metal phase were deposited with variable input energy. Because of the higher melting point of NbC (~3500°C) relative to CPTi (1660°C), higher input energy was required to build any substantial reinforcement between sections of CPTi. Initial attempts to build these structures with four intermediate CPTi layers and a layer-wise transition from 975 J/mm³ to 1075 J/mm³ resulted in high diffusion of NbC into the intermediate CPTi region, and minimal reaction between CPTi and NbC to form *in situ* TiC and Ti-Nb solution. Further process optimization was performed to ensure the distinct metal-ceramic interface from the purely-metallic region. It was found that two consecutive NbC layers and ten intermediate CPTi layers resulted in distinct interfacial regions between the CPTi-NbC reaction zones and the intermediate CPTi deposit (as shown in Fig. 3), substantiating this structure as a truly alternating-material composite having a designed microstructure.

The as-printed structures exhibited unique gradient microstructures along the interface between CPTi and CPTi-NbC reaction zones, with no cracking observed between the particles and the matrix itself (see **Fig. 3**). A transition is observed from the typical "Widmanstatten" [47,48] or acicular-α phase-Ti in the CPTi-deposit to a region containing *in situ* TiC needle-like precipitates that have formed from high temperature reaction between the NbC particles and neighboring titanium during laser processing. Deep within the reaction zone itself, partially-reacted NbC particles and a significant volume fraction of coarse dendrites of *in situ* TiC phase

can be seen, similar to those observed by Savalani et. al (2012) [49]. A smaller volume fraction of lamellar, Ti-Nb β-phase is observed, which is substantiated from EDS analysis that shows a high concentration of both Ti and Nb in the interparticle regions, as well as Nb's BCC-stabilizing relationship to titanium[50]. The presence of all reported phases is substantiated from XRD analysis of the cross section of both reaction zones (Figure 4A), which revealed strong peaks for  $\alpha$ -Ti (40.9° & 46.9°, ICSD:52522), NbC (40.5°, ICSD:181792),  $\beta$ -Ti (45.3°, ICSD:76165), and TiC (42.7° & 49°, ICSD:181681). The fraction of partially-reacted NbC reinforcement within the reaction-zone was estimated to be between 40-75% by volume, when considering area fractions of NbC particles in regions of high apparent reactivity and low apparent reactivity with the titanium matrix. Based on SEM imaging, the overall thickness of the reaction zone ranges from 200µm-250µm. When combined with the size of the overall deposit, this results in 3-3.5vol% NbC reinforcement in the entire structure. Hence, we used 3.5vol%NbC for our control sample. The higher end of the range was chosen as there is an additional complication arising from the fact that the NbC particles in the SEM images are partially reacted, and prior to printing there would have been a slightly higher vol% of unreacted NbC than is observed in the as-printed microstructure. EDS analysis confirms the distinct interface between the titanium composite matrix and the reaction zone via Nb-L mapping, which distinguishes Nb diffusion regions (Ti-Nb solution) and pure CPTi. The cross-sectional hardness profiles show the titanium matrix exhibiting hardness in the 230-250HV<sub>0.2/15</sub> range, and the reaction zone hardness increasing to a range of 400-500 HV<sub>0.2/15</sub>, owing to the *in situ* formed phases (see Figure 4B). NbC particles in this region (>2000HV) were avoided as they posed challenges for obtaining acceptable indents using our setup, meaning that the increase from matrix to reaction zone is strictly due to both the Ti-Nb in situ alloying as well as TiC reinforcement. The CPTi-3.5vol%NbC (not pictured) premixed composition demonstrated a consistent hardness along the build direction between 250 and 350 HV<sub>0.2/15</sub>, indicating an increase in hardness (and subsequent mechanical properties) in comparison to the pure CPTi deposit in the layered structure. From the reaction-zone SEM images of the top surface indentation hardness (as indicated by the schematic in Fig. 4C), the indentation initiated both cracking in the nearby particles as well as further down into the zone, indicating that the matrix in this region has crack-arrest capability, and that the particles are taking on a significant amount of load, both locally and within the larger region, and that cracks

are being arrested in the matrix and particle phases, similar to the nacre image shown in **Fig. 1**. Because the reinforcing NbC particles exhibited strong bonding with the titanium matrix and no processing-induced cracks were observed, the cracking from indentation is attributed to the

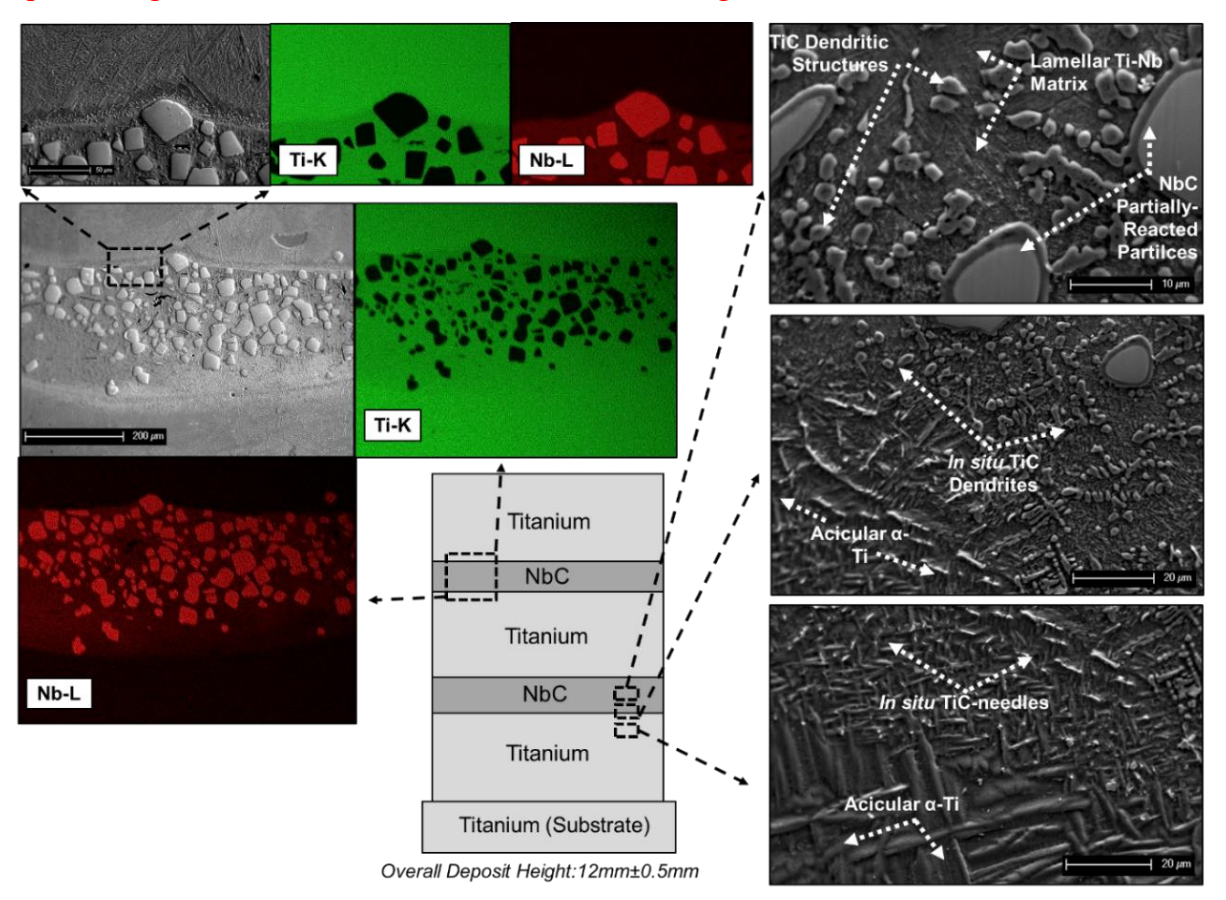
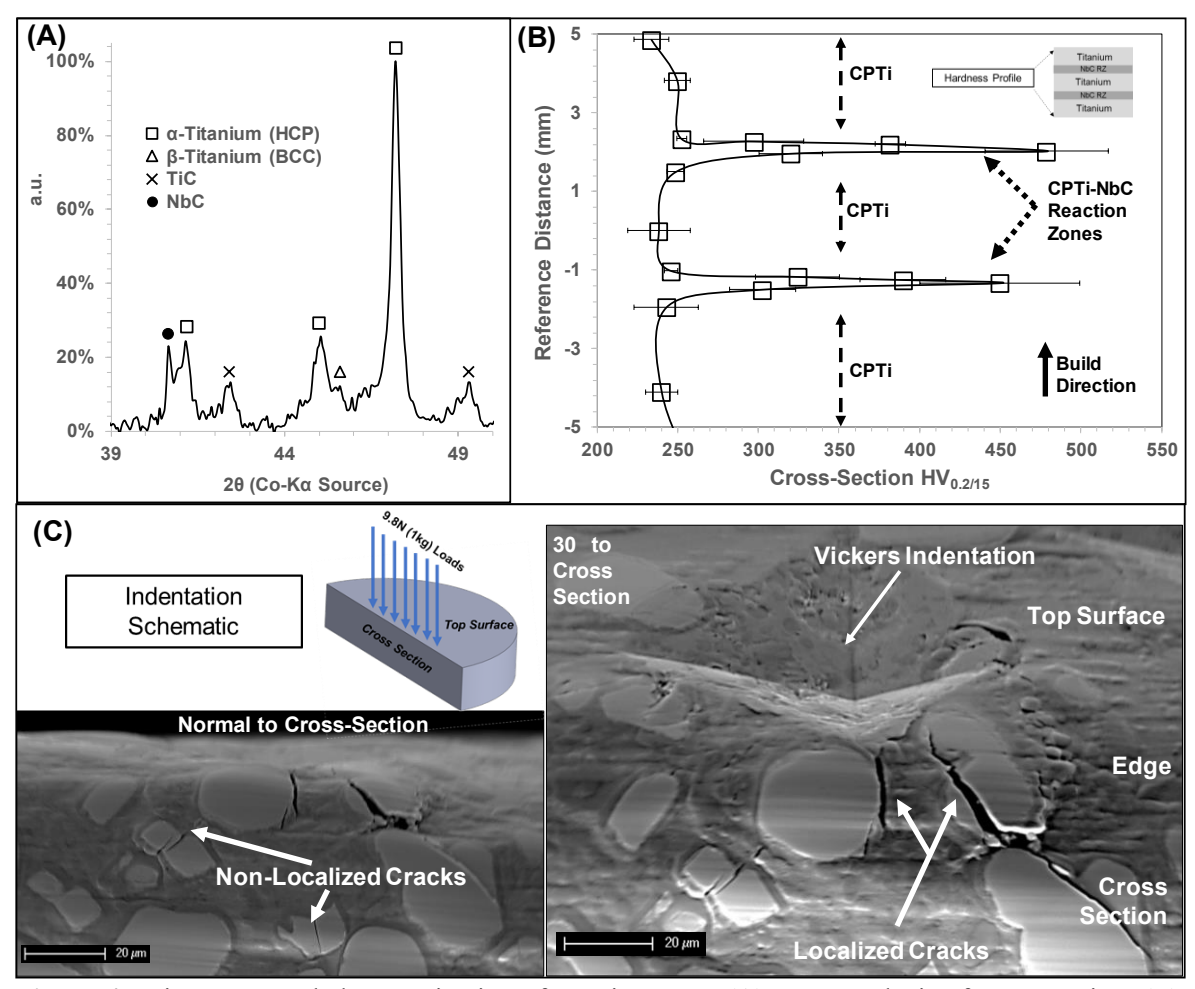


Figure 3: Representative etched-microstructure of the reaction zone (Krolls reagent).

localized loading during indentation.



**Figure 4:** Microstructural characterization of reaction zone. **(A)** XRD analysis of cross section. **(B)** Hardness profile across cross section. **(C)** Localized indentation perpendicular to ground cross section.

The *in situ* reactions that take place during printing are more clearly observed within the premixed, CPTi-3.5vol%NbC composition (**Fig. 5**). Partially-reacted NbC particles, the formation of *in situ* TiC particles along the outer edge, and the embedding of TiC particles within the Ti matrix are observed. Similar microstructure and phase formation are observed nearer to the substrate as well as towards the top portion of the build (shown schematically), indicating that there is minimal effect of thermal (multi-layer) cycling on the overall reactions that take place between the precursor materials. More specifically, the presence of *in situ* phases is mainly dependent upon initial deposition temperature, as opposed to when subsequent layers are being printed. Additionally, TiC particles are observed away from the NbC partially-reacted particles, indicating that there is an area surrounding the particle that is receiving reinforcement

from the *in situ* phases that form, and that the volume reinforcement may in fact be increased in comparison to the powder compositions.

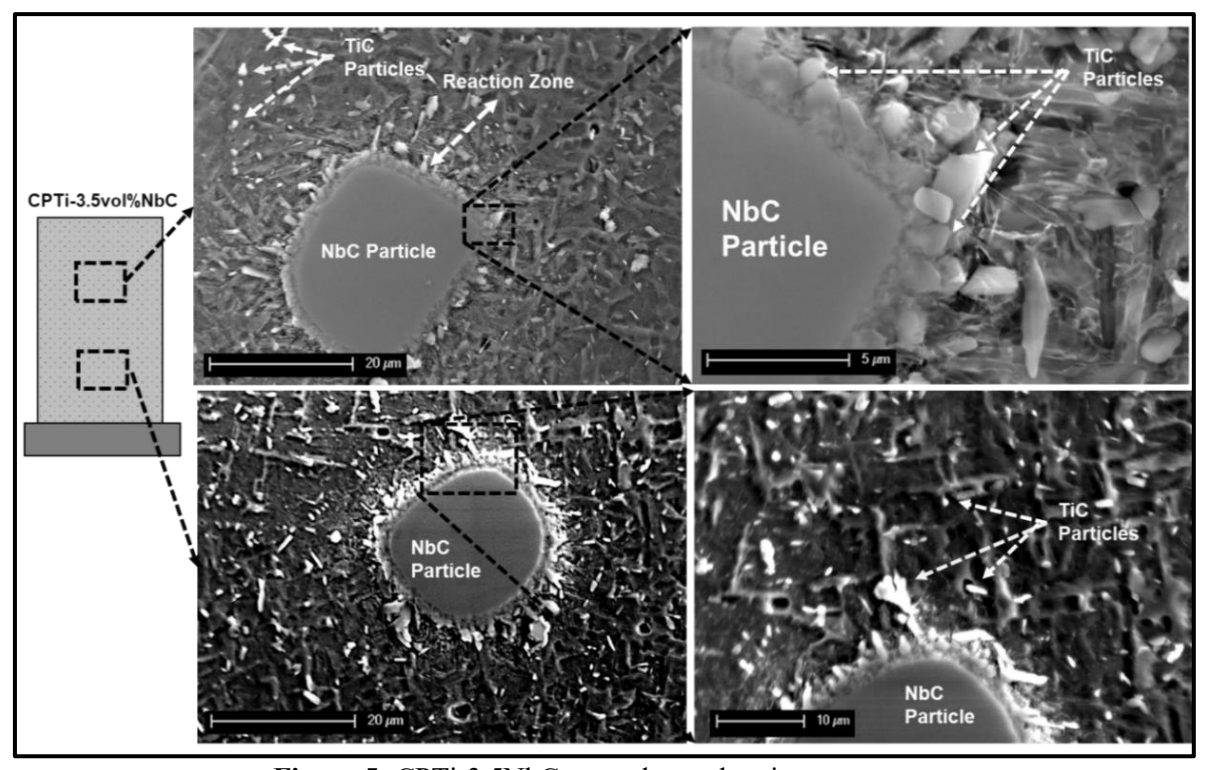


Figure 5: CPTi-3.5NbC control sample microstructures.

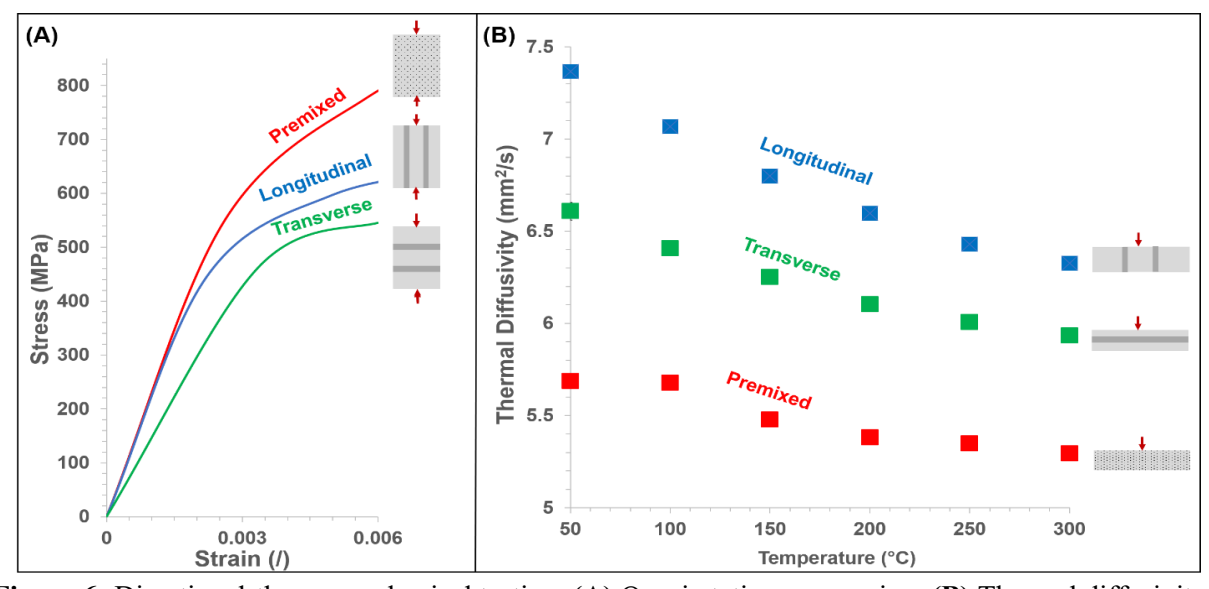
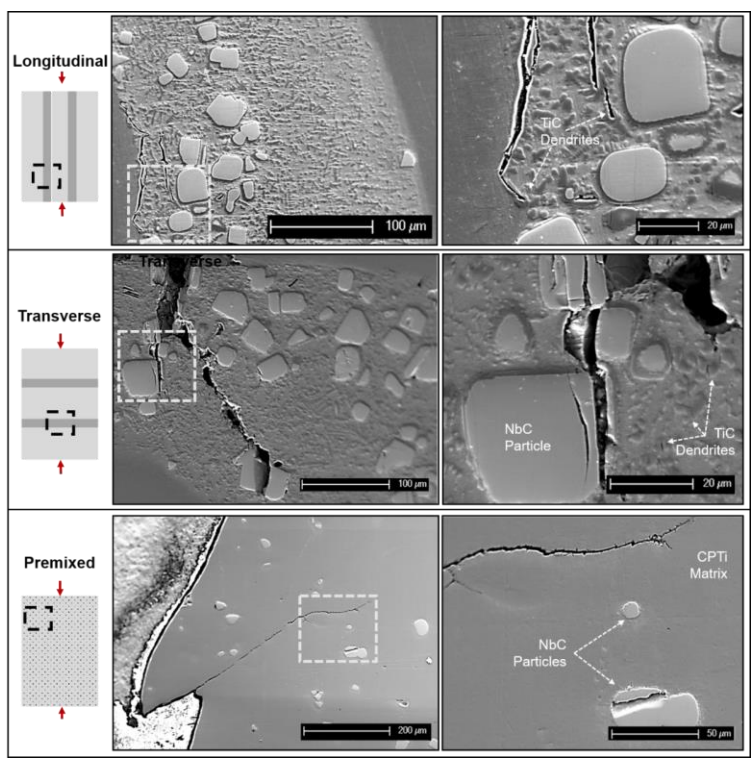


Figure 6: Directional-thermomechanical testing. (A) Quasi-static compression. (B) Thermal diffusivity.

The resulting alternating-metal-ceramic composites showed significant differences in thermomechanical properties between both the loading direction, and compared to the control premixed composite (see Figs. 6-10 & Table 2). The transverse composition demonstrated a



**Figure 7:** Representative damage cross sections from quasistatic compression (unetched).

40% lower modulus compared to the premixed composition (from 230GPa to 140GPa), and 21% lower modulus than the longitudinal build (from 190GPa to 140GPa). In addition, the compressive yield strength demonstrated a similar decreasing trend to the moduli, with strengths of 750MPa, 594MPa, and 538MPa, for the premixed, longitudinal, and transverse directions, respectively. These results indicate these structures' directional-dependence of

compressive deformation, and the tendency for the premixed and longitudinal directions to deform more alike to the reinforcement, and the transverse build more alike to the matrix Ti. All moduli fall within 28% of theoretical values based on composite material theory, which is analyzed further in later sections. The longitudinal loading configuration demonstrated the highest thermal diffusivity, 31% higher than the premixed composition and 10% higher than the single-reaction-zone layer transverse case. All values fell within 16% of theoretical values based on (theoretical) thermal resistance network analysis.

From high strain-rate compressive testing (**Figs. 8 & 9**), the yield strengths were 1159±18MPa, 1025±88MPa, and 922±97MPa, for the premixed, longitudinal, and transverse builds, respectively. In addition, the strains to total failure were 16±1%, 4±1%, and 17±1%, for premixed, longitudinal, and transverse, respectively. These results indicate both this structure's directional-dependence and strain-rate dependence of compressive yield strength and strain to ultimate failure, since the strengths of all compositions are higher than that of the quasi-static deformation. As indicated from both the curves as well as the failure micrographs (**Fig. 10**), the longitudinally-tested composition exhibits very low deformation to failure in comparison to the

transverse and premixed compositions, where both absorb the load and failed in an overall ductile mode. Similarly, representative secondary electron images are shown in Fig. 7 for quasistatic compression crack initiation and propagation along both the interfaces and matrix/reinforcement. For the longitudinal loading case, reinforcing NbC reaction zones exhibited microscale cracks originating near the interface of CPTi and CPTi-NbC reaction zone, but then became arrested through *in situ* TiC dendrites within the reaction zone. The transverse configuration exhibited both small and large-scale cracking originating near the reaction zone interface, propagating through both the CPTi-Nb solution and TiC matrix, while finally being arrested in both NbC particles and *in situ* TiC dendrites. The origin of the crack shown in the transverse configuration came from a printing defect along the top surface of the reaction zone, likely causing localized bending loads that, combined with compressive loading, resulted in crack formation and subsequent propagation. Despite this occurrence, the crack shown was fully arrested before breaching the lower interface, indicating the ability of this structure to withstand loading from defect sites. For the particle-reinforced composite, cracking was exhibited along outer edges, stemming from stress concentrations near the edge of the sample. These cracks

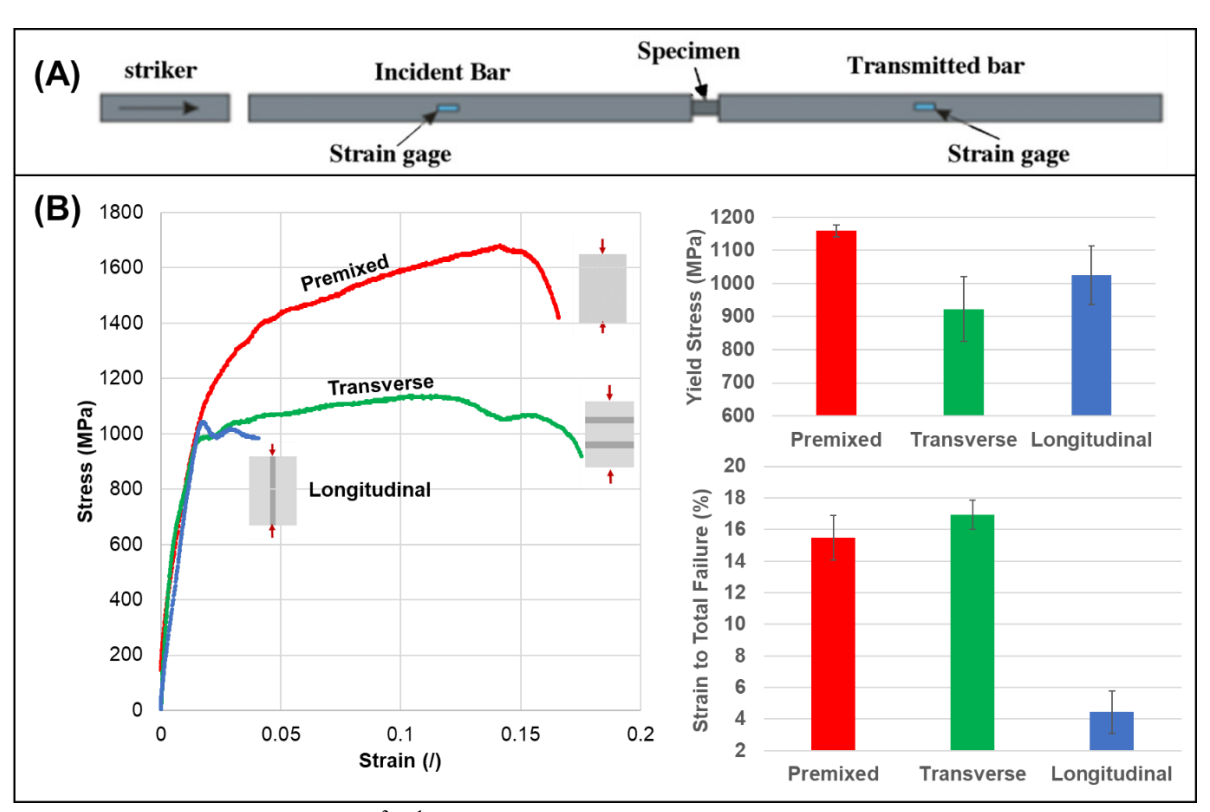


**Figure 8:** High strain-rate ( $\sim 10^3 \text{ s}^{-1}$ ) compression testing of different configurations. **(A)** SHPB setup [44] **(B)** Results from testing.

propagated through the CPTi matrix until they were finally arrested, but resulted in large edge-deformation under loading, as can be seen in **Fig. 7**. Cracks are also observed within the embedded, reinforcing-NbC particle(s) as well as the localized reaction zone, indicating that the NbC particles are taking on a large portion of the load during quasi-static compression.

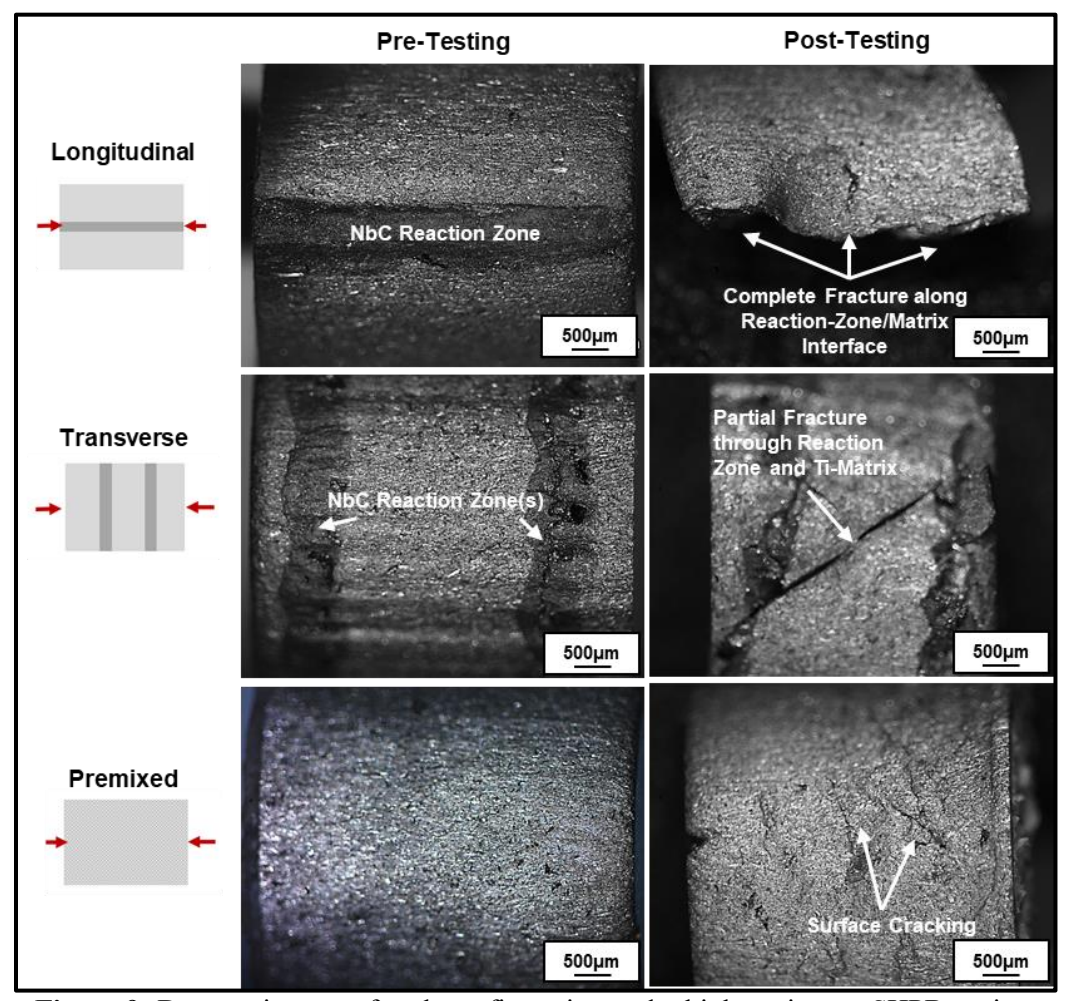


Figure 9: Damage images of each configuration under high strain-rate SHPB testing.

AM has been employed previously to create unique materials and composite structures [12,35,39,51–53], however, herein we have demonstrated a novel variation that allows manufacturers location-specific property control that isn't feasible using traditional methods. More specifically, metal-ceramic alternating-material composites were manufactured with directionally-tailored thermomechanical properties, free of large-scale defects and cracking, and intended for an end-use application requiring a combination of high strength/weight ratio as well as high energy absorption. As the first of its kind, the processing-property relationships, microstructure, and *in situ* phase formations were investigated. Damage evaluation and analysis

was shown to demonstrate the unique customizability of this approach to enhance performance. Many factors influence material behavior during laser-based AM that leads to unique microstructures and properties, which aren't possible with traditional methods. This is especially true for our metal-ceramic composite, where stark differences in melting temperature and mechanical properties of the constituents lead to unique in situ reactions and phase formations [54]. This can be further understood from the input energy applied during the transition from a region of strictly CPTi metal to the CPTi-NbC reaction zone (see Eq. 1 in **Methods** section). For the CPTi regions alone, studies have shown energy densities in the range of 75-500 J/mm<sup>3</sup> evaluated using this same relation[38,55,56], indicating that our optimized value of 325 J/mm<sup>3</sup> is on the higher-end of this processing window. It was found that significantly different input energies were necessary to build on top of the as-deposited CPTi layer and provide effective NbC-particle and in situ phase-reinforcement (325 J/mm<sup>3</sup> for CPTi and 1075 J/mm<sup>3</sup> for NbC). Because of NbC's high-melting temperature and titanium's hightemperature reactivity, NbC deposition resulted in surface re-melting of as-printed titanium as opposed to a pure layer of NbC. Similar reactive-phenomena has been observed during laserprocessing of titanium and titanium-based composites containing various borides, carbides, and nitrides, due to the high reactivity of titanium[32,49,54]. For the Ti-Nb-C material system, Li et al. (2014) demonstrated that during laser cladding, the Gibbs free energy change associated with TiC formation is lower than NbC, showing that it has a higher propensity to form across 300K-1800K[57]. Although our system's precursors are CPTi and NbC powder, it can be envisioned that this analysis extends to the instance where NbC particles are embedded into a surface remelted titanium region, since there is a local abundance of titanium. The formation of TiC then, as shown in the microstructure and phase analysis of Figs. 2-4, is attributed to its higher change in Gibbs free energy within a melt pool containing varying amounts of titanium, niobium, and carbon. Further, any remaining Nb that diffused outwards from the NbC particles formed the β-Ti-Nb solution that was found in the XRD analysis. Although only 40-75% ceramic phase, this reaction zone still had a significant impact on the thermomechanical behavior of the resulting structure, as shown in Fig. 6, and exhibited excellent crack arrest capability under quasi-static compressive loading, as shown in Fig. 7. If this zone were entirely ceramic, this property would be limited, as well as the ability to withstand thermal cycling during laser processing. The formation of TiC and resulting hardness of this region agrees well with studies of Savalani et al.

(2012) who studied *in situ* TiC reinforcement to titanium, demonstrating hardness in the 400-500HV range for 5-10wt%TiC[49]. In addition, the reaction zone top-surface indentation tests (**Fig. 4C**) indicate that this region is well equipped for highly-localized loading as the indentation-initiated cracking that was arrested by both the particles as well as the matrix itself, resulting in cracks both locally in NbC phase as well as further into the reaction zone.

Because of the unique nature of the reaction-zone, modified rule-of-mixtures analysis was used to verify the experimental elastic-modulus and thermal diffusivity of the as-printed composite structures (see **Fig. 10** and **Methods** section). In general, composites will behave in accordance with the relative percentage of phases, but this composite's unique nature requires special considerations. Each of the alternating-material compositions deformed in a monolithic

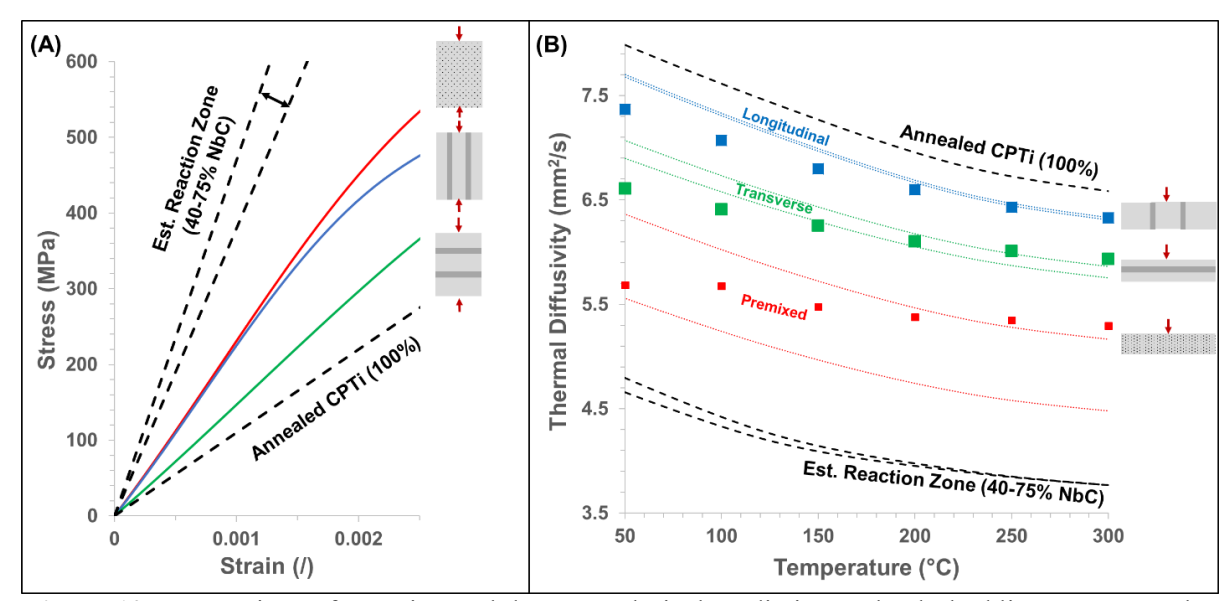


**Figure 10:** Comparison of experimental data to analytical predictions. The dashed lines represent the analytical predictions based on first-principle analysis. **(A)** Quasi-static ompression **(B)** Thermal diffusivity.

material manner in the quasi-static regime, meaning that the main driving factor for variation is the testing direction as well as the estimated vol% NbC reinforcement within the reaction zone. Alternatively, for the premixed CPTi-3.5vol%NbC, the main source of variation is the reactivity between metal-ceramic phases during processing, resulting in non-rule of mixtures behavior due to an effective vol% reinforcement increase from *in situ* TiC and Ti-Nb phases[58]. Compression cracking of the NbC particles also showed the large load-proportion that these reinforcing phases take in the premixed composition. Because of this, our approach involves plotting the compression results for each configuration along with representative (dashed) linear stress-strain

curves for the matrix and estimated reinforcement, to illustrate each configuration's behavior with respect to the base matrix and effective-reinforcement . For thermal diffusivity, the theoretical ranges (dashed lines) are plotted based on the range of NbC reinforcement in the asprinted reaction-zone (i.e. 40-75%), with the reaction-zone range and 100% CPTi on the same plot for reference to reinforcement and matrix properties (see Fig. 10). The effective reaction zone properties are calculated using the 40-75% NbC reinforcement range, with the remaining 25-60% composed of equal parts TiC and Ti-Nb matrix (for ease of calculation). Based on literature values for thermomechanical properties of CPTi [59], CPTi-Nb alloys [60], TiC [61], and NbC [62], this rule of mixtures approximation results in an estimated reaction zone modulus of 380-470 GPa (see Fig. 10), and thermal diffusivity ranging from 4.25 mm²/s to 3.75 mm²/s across 50°C-300°C temperature range. Other properties within this reaction-zone region such as density, specific heat, and thermal conductivity were estimated in a similar manner for calculating the alternating-material composite properties. Because of the non-rule-of mixtures nature of the premixed composite, a range of values for effective volume correction are proposed to help understand the deviation.

Within each tested configuration, estimations for properties of both the alternatingmaterial composites and the premixed composite account for the tested-sample geometry and estimated volume fraction of both the reaction zone(s) as well as in situ phases formed (see Methods section). For the premixed composition, titanium is the matrix and 3.5vol%NbC considered the reinforcement, with a volume correction factor to model the reinforcement volume due to TiC and Ti-Nb solution that causes non-rule of mixtures behavior. These properties result in a range of estimated values, as is shown in Table 2. A value range of 1-1.5 for  $\frac{\Delta R}{R}$  was estimated from imaging of the premixed composition (representative microstructure images are shown in Fig. 3). These values are shown to model both the range of diffusivity and modulus appropriately considering the resulting reaction areas from CPTi and NbC that contain large amounts of TiC and Ti-Nb solution. Both alternating-material composites showed good agreement with experimental results (within 10%), whereas, the premixed composite showed higher variation (under 16.2%) owing to the challenge in modeling its reaction zone and resulting properties, as previously discussed. From Fig. 6B, it is apparent that the longitudinal heat loading direction resembles mostly that of pure CPTi as there are direct heat pathways for CPTi. For the transverse and premixed compositions, the behavior is between pure titanium and NbC because of the reaction zone and thermal barriers presented by *in situ* TiC and NbC particles both in the concentrated reaction zone, as well as the premixed configuration. For thermal diffusivity, theoretical values for all configurations are higher than the experimental, which is attributed to the small grain sizes that stem from high-cooling rate laser processing, creating a thermal barrier effect. This demonstrates that, despite only a fraction of ceramic reinforcement in the reaction zone, there is still a significant effect on the thermal transport properties. The longitudinal loading configuration demonstrated the highest thermal diffusivity, 31% higher than the premixed composition and 10% higher than the single-reaction-zone layer transverse case, demonstrating the difference in directional properties as well as with respect to the premixed composition. It is envisioned that these differences could be further accentuated with additional layers, depending on the intended application.

Overall, the transverse case demonstrated a 40% lower modulus compared to the premixed composition (from 230GPa to 140GPa), and 21% lower modulus than the longitudinal case (from 190GPa to 140GPa), indicating the difference in properties both directionally as well as in comparison to a premixed composition of similar reinforcement. The deviation from experimental data ranges from 9-28%, which is attributed to both estimations made from the reaction zone as well as the variation inherent in additively manufactured components from residual stresses and small grain sizes that can affect the mechanical properties, particularly when using a novel processing method. In comparison to the quasi-static compressive behavior, the high strain-rate curves exhibited variable behavior depending on the configuration (Figs. 8 & 9). In general, all values for strength of each configuration are higher than in the quasi-static regime owing to the strain hardening effect that is common in titanium materials under high strain rate loading [44]. The premixed configuration showed the highest strength owing to the same strengthening mechanisms in the quasi-static regime, while also behaving more as a monolithic material, whereas both the longitudinal and transverse configurations had multiple failure points. As indicated by the failure micrographs from high strain-rate testing, the transverse configuration fails through the titanium and then the reaction-zone(s) resulting in multiple deformation points to ultimate failure. This causes a relatively steady loading across strain as the structure is still withstanding a load during deformation, a desired characteristic among ballistic applications, and commonly observed throughout the literature for processing and properties of different layered composites such as Ti-(SiC<sub>f</sub>/Al3Ti) [24], Ti/Al3Ti [63],

among others [64]. In contrast, the longitudinal configuration fails before further deformation after the first-yield resulting in much lower strain to ultimate failure values, and a catastrophic failure mechanism undesirable under such high strain rate loading. These results indicate that this processing method is capable of producing structures that can withstand high loading in specific directions, and that the failure characteristics can be tailored in comparison to traditionally-processed layered materials, highlighting that natural structural design methodologies can be employed using this fabrication method.

#### **Future Directions**

Based on the thermomechanical performance and compressive damage mechanisms of this alternating-layer composite, process alteration for improved design can be realized (see **Fig.** 

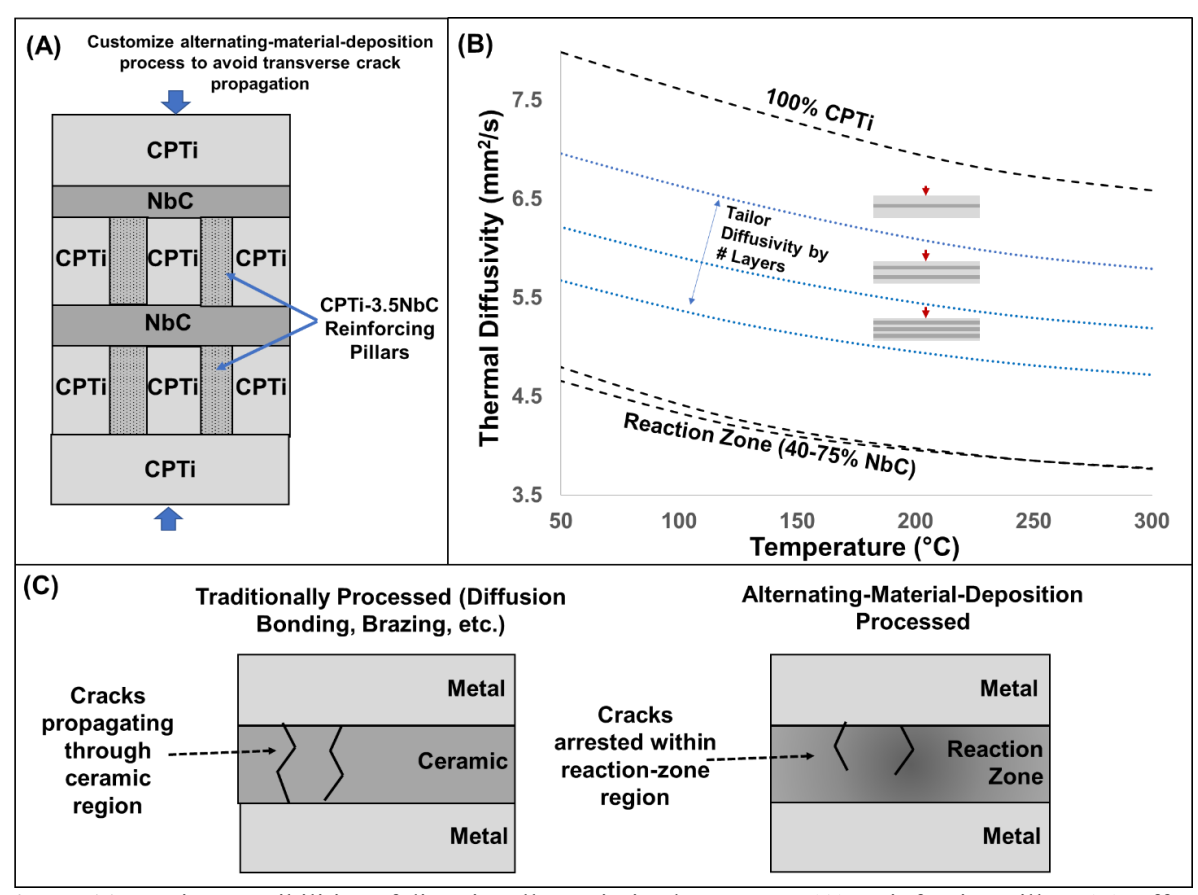


**Figure 11:** Design possibilities of directionally-optimized structures **(A)** Reinforcing pillars **(B)** Effect of the number of reaction zones on the thermal diffusivity **(C)** Crack arrest behavior for traditional vs. alternating-material deposition.

11). Quasi-static crack propagation in the transverse direction, due to combined compressive and bending loads on the reaction zone, could be minimized with the addition of pillar support structures designed and built into the component, as shown in Fig. 11A. While a transition from metallic to ceramic in the present work is accomplished on successive layers, it is important to note that the powder feeder chosen for deposition can change even within the same layer to create pillar-like reinforcement. These pillars could be square or tapered and incorporate a functional gradation from one material to another [19], aiding in buckling mode failure during longitudinal loading. Further, additional reaction zone regions can be implemented for increased control over directional heat transfer. As shown in Fig. 11B, the theoretical transverse diffusivity can be altered significantly with the addition of multiple reaction zones, requiring additional alternating metal-ceramic regions. The reduction of directional heat-transfer through the overall structure may alleviate the issue of adiabatic strain localization that is common in titanium-based materials, limiting their use in ballistic applications. Light-weighting and in situ alloying[25] can also be incorporated to tune the mass and properties by printing regions that utilize a lattice structure design, as well as depositing alloyed titanium powders (such as Ti6Al4V). Further, additional deposit layers of NbC (more than two) can result in even higher-reacted metal-ceramic reaction-zone regions that have further enhanced crack-arrest capability (as shown schematically in Fig. 11C) in comparison to traditionally-processed structures, similar to the damage tolerant mechanisms shown in nacre (Fig. 1). It is envisioned that computational programs will be able to customize this process to meet the needs of many different applications where directional control of thermomechanical properties is of interest.

## **Conclusions**

In this work, directionally tailored metal-ceramic composites have been manufactured to demonstrate that naturally-inspired, architected materials are possible to create using a novel additive manufacturing approach, alleviating much of the challenge of attempting to make these structures in a traditional manner. By leveraging in situ reactivity as well as the ability to change deposited feedstock characteristics in directed energy deposition based processing, composites with as high as 40% difference in directional stiffness and 31% difference in thermal diffusivity were created. In addition, high magnification imaging of damaged samples indicate that the

failure characteristics are improved over what is expected from traditionally-processed composite materials of similar design. As manufacturers and researchers look towards the future of structural design and fabrication, our results demonstrate that they will be able to readily create structures that are hierarchically designed from both composition and architecture standpoints, and reliably replicate them to fully exploit a structure's performance for its intended application.

## **Data Availability**

The raw/processed data required to reproduce these findings cannot be shared at this time as the data also forms part of an ongoing study.

## Acknowledgments

The authors acknowledge experimental support from Jose D. Avila, Bryan Heer, and Dr. Jose Marcial of the N.O.M.E Laboratory at WSU for XRD, and Dr. Jow-lian Ding and Jialong Ning for Split-Hopkinson Pressure Bar testing and analysis at WSU. The authors acknowledge financial support from the National Science Foundation under the grant # CMMI 1538851 (PI-Bandyopadhyay) and #CMMI 1934230 (PI-Bandyopadhyay). Authors also acknowledge financial support from the National Institute of Arthritis and Musculoskeletal and Skin Diseases of the National Institutes of Health under Award Number R01 AR067306-01A1. The content is solely the responsibility of the authors and does not necessarily represent the official views of the National Institutes of Health.

## **Declaration of Interest**

The authors declare no competing interest.

## References

- [1] U. G. K. Wegst, H. Bai, E. Saiz, A. P. Tomsia, R. O. Ritchie, Bioinspired structural materials, Nat. Mater. (2015). doi:10.1038/nmat4089.
- [2] E. Munch, M. E. Launey, D. H. Alsem, E. Saiz, A. P. Tomsia, R. O. Ritchie, Tough, bioinspired hybrid materials, Science (80-.). (2008). doi:10.1126/science.1164865.

- [3] C. Audibert, J. Chaves-Jacob, J.-M. Linares, Q.-A. Lopez, Bio-inspired method based on bone architecture to optimize the structure of mechanical workspieces, Mater. Des. 160 (2018) 708–717. doi:10.1016/j.matdes.2018.10.013.
- [4] M. Rousseau, A. Meibom, M. Gèze, X. Bourrat, M. Angellier, E. Lopez, Dynamics of sheet nacre formation in bivalves, J. Struct. Biol. 165 (2009) 190–195. doi:10.1016/j.jsb.2008.11.011.
- [5] R. O. Ritchie, The conflicts between strength and toughness, Nat. Mater. (2011). doi:10.1038/nmat3115.
- [6] G. X. Gu, F. Libonati, S.D. Wettermark, M.J. Buehler, Printing nature: Unraveling the role of nacre's mineral bridges, J. Mech. Behav. Biomed. Mater. 76 (2017) 135–144. doi:10.1016/j.jmbbm.2017.05.007.
- [7] R. Cunningham, C. Zhao, N. Parab, C. Kantzos, J. Pauza, K. Fezzaa, T. Sun, A.D. Rollett, Keyhole threshold and morphology in laser melting revealed by ultrahigh-speed x-ray imaging, Science (80-.). (2019). doi:10.1126/science.aav4687.
- [8] E. MacDonald, R. Wicker, Multiprocess 3D printing for increasing component functionality, Science (80-.). (2016). doi:10.1126/science.aaf2093.
- [9] S.A.M. Tofail, E.P. Koumoulos, A. Bandyopadhyay, S. Bose, L. O'Donoghue, C. Charitidis, Additive manufacturing: scientific and technological challenges, market uptake and opportunities, Mater. Today. 21 (2018) 22–37. doi:10.1016/j.mattod.2017.07.001.
- [10] T. DebRoy, H.L. Wei, J.S. Zuback, T. Mukherjee, J.W. Elmer, J.O. Milewski, A.M. Beese, A. Wilson-Heid, A. De, W. Zhang, Additive manufacturing of metallic components Process, structure and properties, Prog. Mater. Sci. 92 (2018) 112–224. doi:10.1016/j.pmatsci.2017.10.001.
- [11] D. Bowden, Y. Krysiak, L. Palatinus, D. Tsivoulas, S. Plana-Ruiz, E. Sarakinou, U. Kolb, D. Stewart, M. Preuss, A high-strength silicide phase in a stainless steel alloy designed for wear-resistant applications, Nat. Commun. 9 (2018). doi:10.1038/s41467-018-03875-9.
- [12] B. Onuike, A. Bandyopadhyay, Additive manufacturing of Inconel 718 Ti6Al4V bimetallic structures, Addit. Manuf. 22 (2018) 844–851. doi:10.1016/j.addma.2018.06.025.
- [13] X. Wang, S. Xu, S. Zhou, W. Xu, M. Leary, P. Choong, M. Qian, M. Brandt, Y.M. Xie, S.X. Xiaojian Wang Shiwei Zhou, Wei Xu, Martin Leary, Peter Choong, M. Qian, Milan Brandt, Yi Min Xie., X. Wang, S. Xu, S. Zhou, W. Xu, M. Leary, P. Choong, M. Qian, M. Brandt, Y.M. Xie, S.X. Xiaojian Wang Shiwei Zhou, Wei Xu, Martin Leary, Peter Choong, M. Qian, Milan Brandt, Yi Min Xie., X. Wang, S. Xu, S. Zhou, W. Xu, M. Leary, P. Choong, M. Qian, M. Brandt, Y.M. Xie, Topological design and additive manufacturing of porous metals for bone scaffolds and orthopaedic implants: A review, Biomaterials. 83 (2016) 127–141. doi:10.1016/j.biomaterials.2016.01.012.
- [14] H. Sahasrabudhe, J. Soderlind, A. Bandyopadhyay, Laser processing of in situ TiN/Ti composite coating on titanium, J. Mech. Behav. Biomed. Mater. 53 (2016) 239–249. doi:10.1016/j.jmbbm.2015.08.013.

- [15] M. Das, V.K. Balla, D. Basu, I. Manna, T.S. Sampath Kumar, A. Bandyopadhyay, Laser processing of in situ synthesized TiB-TiN-reinforced Ti6Al4V alloy coatings, Scr. Mater. 66 (2012) 578–581. doi:10.1016/j.scriptamat.2012.01.010.
- [16] S. Tammas-Williams, I. Todd, Design for additive manufacturing with site-specific properties in metals and alloys, Scr. Mater. 135 (2017) 105–110. doi:10.1016/j.scriptamat.2016.10.030.
- [17] B. H. Jared, M.A. Aguilo, L.L. Beghini, B.L. Boyce, B.W. Clark, A. Cook, B.J. Kaehr, J. Robbins, Additive manufacturing: Toward holistic design, Scr. Mater. 135 (2017) 141–147. doi:10.1016/j.scriptamat.2017.02.029.
- [18] T. Slawik, A. Bergner, R. Puschmann, P. Franke, J. Raethel, T. Behnisch, R. Scholl, L.-M.M. Berger, T. Moritz, R. Zelm, M. Gude, A. Michaelis, E. Beyer, C. Leyens, H. Grobmann, B. Kieback, H. Großmann, B. Kieback, H. Grobmann, B. Kieback, Metalceramic layered materials and composites manufactured using powder techniques, Adv. Eng. Mater. 16 (2014) 1293–1302. doi:10.1002/adem.201400221.
- [19] C.-Y. Huang, Y.-L. Chen, Design and impact resistant analysis of functionally graded Al2O3–ZrO2 ceramic composite, Mater. Des. 91 (2016) 294–305. doi:10.1016/j.matdes.2015.11.091.
- [20] I. G. Crouch, Body armour New materials, new systems, Def. Technol. (2019). doi:10.1016/j.dt.2019.02.002.
- [21] G. B. Sinclair, J.E. Helms, A review of simple formulae for elastic hoop stresses in cylindrical and spherical pressure vessels: What can be used when, Int. J. Press. Vessel. Pip. 128 (2015) 1–7. doi:10.1016/j.ijpvp.2015.01.006.
- [22] V. Kumar, K. Balasubramanian, Progress update on failure mechanisms of advanced thermal barrier coatings: A review, Prog. Org. Coatings. 90 (2016) 54–82. doi:10.1016/j.porgcoat.2015.09.019.
- [23] E. Medvedovski, Ballistic performance of armour ceramics: Influence of design and structure. Part 1, Ceram. Int. 36 (2010) 2103–2115. doi:10.1016/j.ceramint.2010.05.021.
- [24] C. Lin, Y. Han, C. Guo, Y. Chang, X. Han, L. Lan, F. Jiang, Synthesis and mechanical properties of novel Ti-(SiCf/Al3Ti) ceramic-fiber-reinforced metal-intermetallic-laminated (CFR-MIL) composites, J. Alloys Compd. 722 (2017) 427–437. doi:10.1016/j.jallcom.2017.06.057.
- [25] K. D. Traxel, A. Bandyopadhyay, Reactive-deposition-based additive manufacturing of Ti-Zr-BN composites, Addit. Manuf. 24 (2018). doi:10.1016/j.addma.2018.10.005.
- [26] Y. Zhang, A. Bandyopadhyay, Direct Fabrication of Compositionally Graded Ti-Al2O3 Multi-Material Structures using Laser Engineered Net Shaping, Addit. Manuf. 21 (2018) 104–111. doi:10.1016/j.addma.2018.03.001.
- [27] T. Gualtieri, A. Bandyopadhyay, Additive manufacturing of compositionally gradient metal-ceramic structures: Stainless steel to vanadium carbide, Mater. Des. 139 (2018) 419–428. doi:10.1016/j.matdes.2017.11.007.

- [28] M. Garcia-Avila, M. Portanova, A. Rabiei, Ballistic Performance of a Composite Metal Foam-ceramic Armor System, Procedia Mater. Sci. 4 (2014) 151–156. doi:10.1016/j.mspro.2014.07.571.
- [29] C. Tian, X. An, Q. Sun, Y. Dong, Experimental and numerical analyses of the penetration resistance of ceramic-metal hybrid structures, Compos. Struct. 211 (2019) 264–272. doi:10.1016/j.compstruct.2018.12.021.
- [30] B. McWilliams, J. Yu, M. Pankow, C.-F. Yen, Ballistic impact behavior of woven ceramic fabric reinforced metal matrix composites, Int. J. Impact Eng. 86 (2015) 57–66. doi:10.1016/j.ijimpeng.2015.07.005.
- [31] T. Gualtieri, A. Bandyopadhyay, Niobium carbide compostie coatings on SS304 using laser engineered net shaping (LENS<sup>TM</sup>), Mater. Lett. 189 (2017) 89–92. doi:10.1016/j.matlet.2016.11.071.
- [32] S. Pouzet, P. Peyre, C. Gorny, O. Castelnau, T. Baudin, F. Brisset, C. Colin, P. Gadaud, Additive layer manufacturing of titanium matrix composites using the direct metal deposition laser process, Mater. Sci. Eng. A. 677 (2016) 171–181. doi:10.1016/j.msea.2016.09.002.
- [33] W. Chen, C. Chen, X. Zi, X. Cheng, X. Zhang, Y.C. Lin, K. Zhou, Controlling the microstructure and mechanical properties of a metastable β titanium alloy by selective laser melting, Mater. Sci. Eng. A. 726 (2018) 240–250. doi:10.1016/j.msea.2018.04.087.
- [34] M. Fischer, D. Joguet, G. Robin, L. Peltier, P. Laheurte, In situ elaboration of a binary Ti-26Nb alloy by selective laser melting of elemental titanium and niobium mixed powders, Mater. Sci. Eng. C. 62 (2016) 852–859. doi:10.1016/j.msec.2016.02.033.
- [35] H. Sahasrabudhe, A. Bandyopadhyay, Additive Manufacturing of Reactive In Situ Zr Based Ultra-High Temperature Ceramic Composites, Jom. 68 (2016) 822–830. doi:10.1007/s11837-015-1777-x.
- [36] A. Uriondo, M. Esperon-Miguez, S. Perinpanayagam, The present and future of additive manufacturing in the aerospace sector: A review of important aspects, Proc. Inst. Mech. Eng. Part G J. Aerosp. Eng. 229 (2015) 2132–2147. doi:10.1177/0954410014568797.
- [37] J.-P. Kruth, P. Mercelis, J. Van, V.L. Froyen, M. Rombouts, J. Van Vaerenbergh, L. Froyen, Binding mechanisms in selective laser sintering and selective laser melting Binding mechanisms in selective laser sintering and selective laser melting, Rapid Prototyp. J. Rapid Prototyp. J. Rapid Prototyp. J. 11 (2005) 26–36. http://dx.doi.org/10.1108/13552540510573365%0Ahttp://dx.doi.org/10.1108/RPJ-12-2011-0127%0Ahttp://dx.doi.org/10.1108/13552541011083371.
- [38] H. Attar, M. Calin, L.C. Zhang, S. Scudino, J. Eckert, Manufacture by selective laser melting and mechanical behavior of commercially pure titanium, Mater. Sci. Eng. A. 593 (2014) 170–177. doi:10.1016/j.msea.2013.11.038.
- [39] B. Onuike, B. Heer, A. Bandyopadhyay, Additive manufacturing of Inconel 718—Copper alloy bimetallic structure using laser engineered net shaping (LENS<sup>TM</sup>), Addit. Manuf. 21 (2018) 133–140. doi:10.1016/j.addma.2018.02.007.

- [40] ASTM Standard E384-16, Test Method for Microindentation Hardness of Materials, ASTM International, West Conshohocken, PA, PA, 2016. doi:10.1520/E0384-16.
- [41] ASTM Standard C1327, W. Conshohocken, ASTM Standard C1327, Test Method for Vickers Indentation Hardness of Advanced Ceramics, ASTM International, West Conshohocken, PA, PA, 2015. doi:10.1520/C1327-08.2.
- [42] ASTM Standard E9-09, Standard Test Methods of Compression Testing of Metallic Materials at Room Temperature, Annu. B. ASTM Stand. 3.01 (2012) 92–100. doi:10.1520/E0009-09.2.
- [43] R. F. Gibson, R.F. Givson, Principles of Composite Material Mechanics, Isbn0070234515 9780070234512. (2012). doi:10.2214/ajr.159.6.1442392.
- [44] N. Biswas, J.L. Ding, V.K. Balla, D.P. Field, A. Bandyopadhyay, Deformation and fracture behavior of laser processed dense and porous Ti6Al4V alloy under static and dynamic loading, Mater. Sci. Eng. A. 549 (2012) 213–221. doi:10.1016/j.msea.2012.04.036.
- [45] I. Barin, Thermochemical Data of Pure Substances, VCH, New York, NY (USA), NY (USA), 1995.
- [46] Y. A. Cengel, A. J. Ghajar, Heat and Mass Transfer, Fundamentals & Application, Fifth Edition in SI Units, 2015. http://www.osti.gov/energycitations/product.biblio.jsp?osti\_id=6008324.
- [47] E. W. Collings, The Physical Metallurgy of Titanium Alloys, ASM Series in Metal Processing, 1986.
- [48] H. Attar, K.G. Prashanth, A.K. Chaubey, M. Calin, L.C. Zhang, S. Scudino, J. Eckert, Comparison of wear properties of commercially pure titanium prepared by selective laser melting and casting processes, Mater. Lett. 142 (2015) 38–41. doi:10.1016/j.matlet.2014.11.156.
- [49] M. M. Savalani, C.C. Ng, Q.H. Li, H.C. Man, In situ formation of titanium carbide using titanium and carbon-nanotube powders by laser cladding, Appl. Surf. Sci. 258 (2012) 3173–3177. doi:10.1016/j.apsusc.2011.11.058.
- [50] American Society for Metals, ASM Handbook-Vol 3-Alloy Phase Diagrams, 1992. doi:10.1007/BF02869318.
- [51] A. Bandyopadhyay, B. Heer, Additive manufacturing of multi-material structures, Mater. Sci. Eng. R Reports. 129 (2018) 1–16. doi:10.1016/j.mser.2018.04.001.
- [52] D. C. Hofmann, S. Roberts, R. Otis, J. Kolodziejska, R.P. Dillon, J.O. Suh, A.A. Shapiro, Z.K. Liu, J.P. Borgonia, Developing gradient metal alloys through radial deposition additive manufacturing, Sci. Rep. 4 (2014). doi:10.1038/srep05357.
- [53] D. C. Hofmann, J. Kolodziejska, S. Roberts, R. Otis, R.P. Dillon, J.-O. Suh, Z.-K. Liu, J.-P. Borgonia, Compositionally graded metals: A new frontier of additive manufacturing, J. Mater. Res. 29 (2014) 1899–1910. doi:10.1557/jmr.2014.208.
- [54] M. Das, K. Bhattacharya, S.A. Dittrick, C. Mandal, V.K. Balla, T.S. Sampath Kumar, A.

- Bandyopadhyay, I. Manna, In situ synthesized TiB-TiN reinforced Ti6Al4V alloy composite coatings: Microstructure, tribological and in-vitro biocompatibility, J. Mech. Behav. Biomed. Mater. 29 (2014) 259–271. doi:10.1016/j.jmbbm.2013.09.006.
- [55] D. Gu, Y.C. Hagedorn, W. Meiners, G. Meng, R.J.S. Batista, K. Wissenbach, R. Poprawe, Densification behavior, microstructure evolution, and wear performance of selective laser melting processed commercially pure titanium, Acta Mater. 60 (2012) 3849–3860. doi:10.1016/j.actamat.2012.04.006.
- [56] B. Wysocki, P. Maj, A. Krawczyńska, K. Rożniatowski, J. Zdunek, K.J. Kurzydłowski, W. Święszkowski, Microstructure and mechanical properties investigation of CP titanium processed by selective laser melting (SLM), J. Mater. Process. Technol. 241 (2017) 13–23. doi:10.1016/j.jmatprotec.2016.10.022.
- [57] Q. Li, Y. Lei, H. Fu, Growth mechanism, distribution characteristics and reinforcing behavior of (Ti, Nb)C particle in laser cladded Fe-based composite coating, Appl. Surf. Sci. (2014). doi:10.1016/j.apsusc.2014.08.052.
- [58] J.J. Sobczak, L. Drenchev, Metallic Functionally Graded Materials: A Specific Class of Advanced Composites, J. Mater. Sci. Technol. 29 (2013) 297–316. doi:10.1016/j.jmst.2013.02.006.
- [59] K. Firm, R. Boyer, G. Welsch, Materials Properties Handbook: Titanium Alloys, 1994. doi:http://www.sciencedirect.com/science/article/pii/S0045782504000313.
- [60] 55Ti-45Nb Alloy Datasheet, MatWeb Mater. Mater. Prop. Data, from ATI Wah Chang. (n.d.). http://www.matweb.com/search/datasheet.aspx?MatGUID=d4a84f06d085480389dfde4f5e 62d6e4 (accessed August 20, 2010).
- [61] M. Bauccio, ASM engineered materials reference book, 1994.
- [62] D.R. Lide, CRC Handbook of Chemistry and Physics, 84th Edition, 2003-2004, Handb. Chem. Phys. (2003). doi:10.1136/oem.53.7.504.
- [63] Y. Cao, C. Guo, S. Zhu, N. Wei, R.A. Javed, F. Jiang, Fracture behavior of Ti/Al3Ti metal-intermetallic laminate (MIL) composite under dynamic loading, Mater. Sci. Eng. A. 637 (2015) 235–242. doi:10.1016/j.msea.2015.04.025.
- [64] V. V Skorokhod, SECOND INTERNATIONAL CONFERENCE "MATERIALS AND COATINGS UNDER EXTREMAL CONDITIONS" LAYERED COMPOSITES: STRUCTURAL CLASSIFICATION, THERMOPHYSICAL AND MECHANICAL PROPERTIES, 2003.